

# GRAPH BASED METHODS FOR BRAIN STRUCTURAL CONNECTIVITY ANALYSIS

Nemo Fournier

Supervised by Pierre Maurel and Julie Coloigner

I studied brain connectivity analysis, with an emphasis on graph based methods. I adapted a recent measure to compare connectivity networks across subjects, based on graph signal processing and optimal transport ideas. I extended it by introducing a new way to leverage information from a whole cohort of subjects: barycenter computation. I also studied another tool, graph curvature, for which I proposed an adaptation to our context.

## Contents

|  |           |
|--|-----------|
| Introduction   | 2         |
| <b>1. Connectivity</b>   | <b>3</b>  |
| 1.1. Nature of Brain Connectivity . . . . .                      | 3         |
| 1.2. Why Study Brain Connectivity? . . . . .                     | 5         |
| 1.3. State of the Art of Connectome Comparison .                 | 6         |
| <b>2. Graph Signal Processing and Optimal Transport</b>          | <b>7</b>  |
| 2.1. Graph Signals . . . . .                                     | 7         |
| 2.2. Optimal Transport of Smooth Graph Signals                   | 12        |
| 2.3. Wasserstein Distance on our Connectivity Matrices . . . . . | 13        |
| 2.4. Barycenters of Gaussian distributions . . . . .             | 14        |
| 2.5. Barycenters for Connectivity Analysis . . . . .             | 16        |
| <b>3. Graph Curvature</b>  | <b>18</b> |
| 3.1. From Riemannian manifolds to networks . .                   | 18        |
| 3.2. Ollivier-Ricci Curvature on Connectivity Graphs             | 23        |
| Conclusion   | 24        |

|  |    |
|--|----|
| A. Introduction on Optimal Transport                           | 26 |
| B. Remerciements et Contexte Institutionnel et Social du Stage | 29 |

## Introduction

Analysing *brain connectivity* aims at studying how each region of the brain relates to each other. In the last decades, the improvement of non-invasive acquisition techniques has significantly broadened our capability to capture fine details about either physical or functional connections in the brain. Their diffusion among research centres has made connectivity analysis one of the spearheads of neuroscience studies. There is good hope that a better understanding of the brain's behaviour can come out of it.

I will present the different notions of connectivity in section 1, as well as their uses and the challenges arising from their analysis. The aim of my work is to develop a new metric to *compare* connectivity across subjects.

To this end, I will introduce the framework of *graph signal processing* in section 2. It has already found promising applications in the wider field of complex network analysis. We adapted a recently proposed metric to our setting, combining ideas from graph signal processing and the theory of *optimal transportation* (I introduce the tools of optimal transport as needed along the document, but a more comprehensive introduction is provided in appendix A for the interested reader). I proposed an extension of this metric, by exploiting a notion of barycenter which allows for comparisons of cohorts instead of individuals.

I apply the methods that I adapt and devise to data acquired for the study of depression. This data was collected in Rennes from patients suffering from mood depressive disorder to investigate the long term effects of the pathology on the brain as well as biomarkers of clinical aspects of the disease, such as drug-resistance. In this report, I will refer to *patients* for subjects suffering from depression, and *controls* for the healthy group.

I then studied another notion, *graph curvature*, that provides a new way to unveil the structural information of a graph. I describe its foundations in section 3, and I discuss how we could adapt it in our context. I present a new idea for its computation using a *diffusion distance*, as well as some preliminary results obtained with the aforementioned data.

Most of the implementations that I produced during this in-

ternship are available online<sup>\*</sup>. I have also had the opportunity to contribute to the Python Optimal Transport library, that I used for some of my implementations, and I have been part of a paper submission to JMLR as a contributor of this library.

## 1. Connectivity

Studying human *brain connectivity* is all about understanding how the brain processes information. The physiology of its microstructure — neurons interconnected via axons and communicating through synaptic action potentials — is well understood at the scale of individual cells. Yet the organ's sophistication (tens of billions of neurons, about  $10^{14}$  synapses) prohibits its study at the scale of individual neurons, especially when it comes to explaining its complex behaviours.

We can nevertheless consider studying it as a whole system by relying on the hypothesis that the brain's organization at a macro-scale (where atomic elements are populations of neurons instead of individual cells) allows for an overall efficient processing of information. Under this assumption, observing it at this macro-level should still convey meaningful insights.

A landmark paper in this field is an article of Sporns, Tononi, and Kötter<sup>†</sup>, in which they coin the term *connectonomic* for the study of the physical organization of the brain. It has been shown that the macro-scale is indeed a relevant scale. Similarly to other complex-networks, such as social or biological networks, properties of information segregation (segmentation of the brain into highly specialised areas) and integration (with a global communication scheme between those specialised areas), as well as small-worldness or resilience have been described. This network is referred to as the *human connectome*.

<sup>†</sup> Sporns et al. (2005)

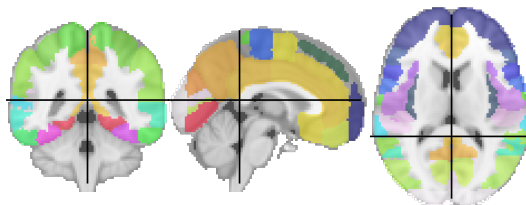


**Figure 1:** Harvard-Oxford Atlas, showing how the brain can be segmented into specialised areas.

### 1.1. Nature of Brain Connectivity

Brain connectivity analysis can be divided into two main subdomains whose distinction lies in the nature of the studied network.

<sup>\*</sup> <https://github.com/little-nem/brain-connectivity-analysis>

On the one hand, there is the study of *functional connectivity*, which involves measuring the activity of the brain and understanding how different areas interact with each other. This can especially provide insights about how the brain behaves while performing some given cognitive task. On the other hand, *structural connectivity* can also be investigated. Here, we are heedful of the physical organization of the brain, which we infer from the observation of brain matter.

In both cases, we aim at defining a notion of connectivity in the brain, that accounts for how much each region of the brain interacts or is linked with each other. I will introduce in the next paragraphs the main ideas behind data acquisition in both contexts.

### **Functional connectivity**

The main tool used to measure functional connectivity is Functional Magnetic Resonance Imaging (fMRI). This is an imaging technique introduced in the 1990s aiming at measuring brain activity. In its most widespread form, it exploits the fact that active neurons need oxygen, and will thus be supplied by a flow of oxygen-saturated blood. This exchange of oxygen induces perturbations in the magnetic properties of the tissues, which we can measure and localize both in space and time. An fMRI session thus results in a collection of time series, each associated with the absolute activity of a confined geographic region of the brain. One of the possible interpretations of the data comes from correlations between the measured activity of different parts of the brain. This allows defining the functional connectivity of the brain, describing a network in which parts of the brain with correlated activities are deemed connected.

### **Structural connectivity**

It is possible to unveil the physical structure of the brain through Diffusion Magnetic Resonance Imaging. In order to establish a map of the physical connections channels, this technique involves measuring diffusion patterns of water molecules in the brain. Those indirectly reveal the structure of brain fibers, since water molecules are more likely to diffuse following those fibers. This leads to the computation of a *tractogram* from which we can derive a network-like structure of the brain, where physical fiber connects the areas they go through. The pipeline to extract the networks we will be working with is visually represented in figure

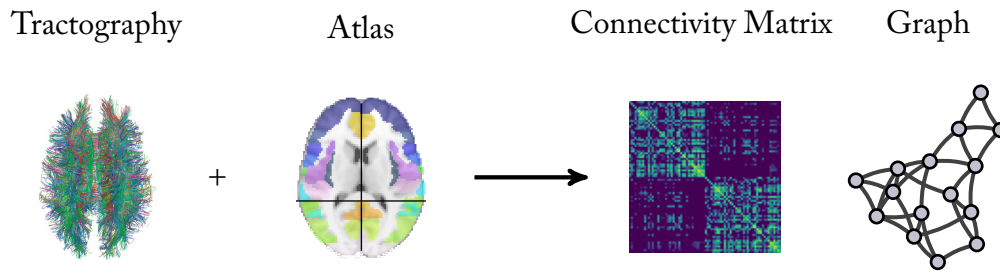


**Figure 2:** Classical structural connectivity pipeline. A tractography is acquired through diffusion MRI. We use an atlas (in our study the Freesurfer atlas, defining 80 regions) to compute a connectivity matrix: each entry is the number of fibers (obtained from the tractography) between two of the regions defined by the atlas. We can also compute the associated connectivity graph, which is such that its adjacency matrix is the connectivity matrix. (Tractography picture by Xavier Gigandet)

## 1.2. Why Study Brain Connectivity?

Brain connectivity analysis has already provided some promising results, showing that the instruments used to infer brain networks from actual subjects and to capture fine details about the brain's organization. Here are some active research topics for which the study of brain connectivity analysis has provided insights:

- ▶ Identify structures responsible for given cognitive functions and establish a “map” of the human connectome. See for example the Human Connectome Project (HCP)<sup>2</sup>.
- ▶ Identify alterations in the connectome that could be markers of pathologies. For instance modifications of connectome topology have been observed in schizophrenia<sup>3</sup> or depression<sup>4</sup>. Studies are now more focused on smaller biomarkers, *e.g.* drug-resistance, pathology phenotypes
- ▶ Record changes in the connectome along time, caused by ageing, a pathology, or a treatment. For instance, Dosenbach et al.<sup>5</sup> uses support vector regressions to compute a “maturation index” from the strength of connections in the connectome, which can be used to predict the age of a subject. More recently, Wen et al.<sup>6</sup> used deep learning approaches to achieve a similar goal.
- ▶ Perform subject identification using connectivity maps as fingerprints, as is done in Venkatesh, Jaja, and Pessoa<sup>7</sup> using nearest-neighbours predictors in a geodesic subspace of matrices.
- ▶ Map functional and structural connectivity, *i.e.* understand how both of them actually relate and if we can infer one notion of connectivity from the other. See for example Hosseini and Kesler<sup>8</sup> or Meier et al.<sup>9</sup>

<sup>2</sup> Van Essen et al. (2013)

<sup>3</sup> Bassett et al. (2008)

<sup>4</sup> Coloigner et al. (2018)

<sup>5</sup> Dosenbach et al. (2010)

<sup>6</sup> Wen et al. (2019)

<sup>7</sup> Venkatesh et al. (2019)

<sup>8</sup> Hosseini et al. (2013)

<sup>9</sup> Meier et al. (2016)

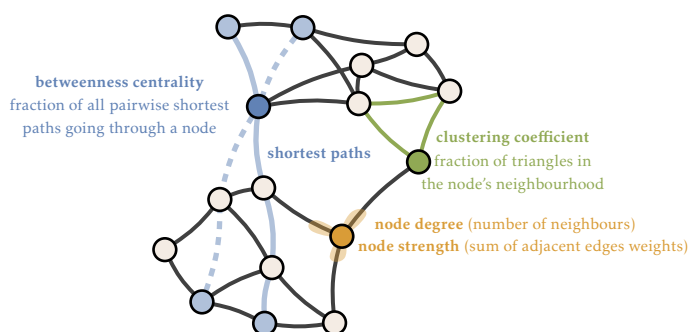
A key element of those analyses is the ability to *compare* con-

nectivity networks between subjects or across time (in the case of a longitudinal study), and explicit the meaningful differences between connectomes. This can help to account for individual variability among subjects, reveal differences between two cohorts, etc.

### 1.3. State of the Art of Connectome Comparison

The representation of connectomes through their connectivity matrix is often encountered in articles because it is especially efficient for visual comparison of connectomes: Alper et al.<sup>10</sup> shows that information is harder to extract visually from connectivity graph representations. Multiple studies have developed principles to compare connectivity matrices. Standard matricial norms have been used, such as the  $l_2$  difference norm<sup>11</sup> or the Pearson correlation between vectorized matrices<sup>12</sup>. More refined approaches exploit algebraic properties of connectivity maps to derive relevant notions of distance. For instance, in Venkatesh, Jaja, and Pessoa<sup>7</sup>, functional connectivity maps are proved to live in a submanifold of  $\mathbf{R}^{n \times n}$  in which a geodesic distance can be defined and provides more reliable results than distances defined in the full matrix space. The ideas behind this approach are summed up in figure 3.

Exploiting the duality between a connectivity matrix and the associated network, a trend in connectivity analysis is to embrace complex network inspired measures. This often involves computing several topological properties of the graph, ranging from individual node strengths to clustering coefficients as well as average shortest path lengths. An in-depth review of those markers can be found in Rubinov and Sporns<sup>13</sup>, and I present some of them in figure 4. Most of those measures can find meaningful interpretations in terms of local network resilience, modularity, etc. They take part for example to the analysis conducted in Coloigner et al.<sup>4</sup> or Mheich, Wendling, and Hassan<sup>14</sup> where they are used to identify differences between cohorts.



<sup>10</sup> Alper et al. (2013)

<sup>11</sup> Ponsoda et al. (2017)

<sup>12</sup> Finn et al. (2015)

<sup>7</sup> Venkatesh et al. (2019)

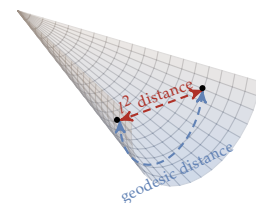


**Figure 3:** Functional connectivity matrices can be shown to live in conic submanifold of  $\mathbf{R}^{n \times n}$ . Distances can be computed by taking this structure into account, as in Venkatesh, Jaja, and Pessoa<sup>7</sup>.

<sup>13</sup> Rubinov et al. (2010)

<sup>4</sup> Coloigner et al. (2018)

<sup>14</sup> Mheich et al. (2019)

**Figure 4:** Some topologic markers used in complex network analysis.

<sup>15</sup> Xiang et al. (2019)

<sup>16</sup> Ricaud et al. (2019)

## 2.1. Graph Signals

It is interesting to see that a time series is a particular graph signal, for which the support graph is a path where each node corresponds to a time sample. This is illustrated in figure 5.

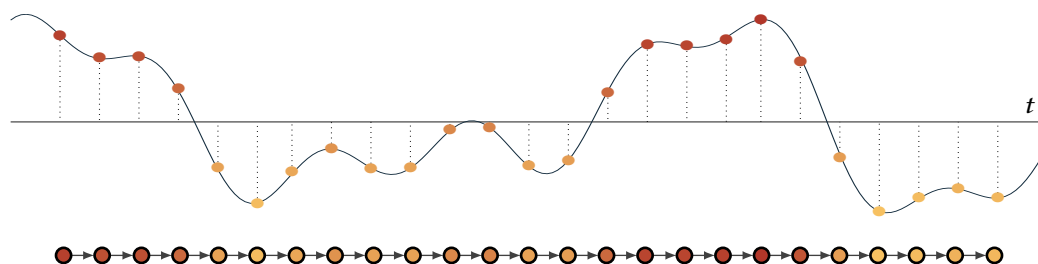


**Figure 5:** A time series and its graph counterpart. The value of the signal on the graph is represented using colors on nodes, yellow being a low value, and red a high one



## Deriving Tools for the Analysis of Signals on Graphs

It will be convenient to adopt a matricial perspective on the different objects that we manipulate. We can see a set of nodes  $V = \{v_1, \dots, v_n\}$  as the standard basis of the space  $\mathbf{R}^n$ . A signal on a graph can thus be expressed as a vector  $s = (s_1 \dots s_n)^\top$  of  $\mathbf{R}^n$ , such that its coordinates are the value of the signal at each node. The adjacency matrix  $A$  of the graph is the matrix such that  $A_{i,j} = 1$  if  $i$  and  $j$  are linked by an edge. The set of edges  $E = \{e_1, \dots, e_p\}$  can also be seen as the standard basis of  $\mathbf{R}^p$ . Those objects are illustrated in figure 6.

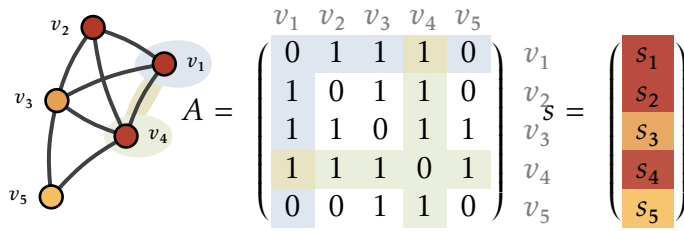


**Figure 6:** Graph with a signal defined on it (represented by the color on the nodes, red for a high value and yellow for a low one), its adjacency matrix  $A$ , and the signal vector  $s$ .

At this point, we will suppose that the graph is oriented, which means that each edge  $(i, j)$  leaves a vertex  $(i)$  to enter the other  $(j)$ . We will see later that the orientation does not matter for what we are interested in, but it eases the intuition behind the next objects we will introduce. To account for this orientation, we introduce the *incidence matrix* of the graph. It is the matrix of the application from  $\mathbf{R}^p$  to  $\mathbf{R}^n$  expressed in the bases  $E$  and  $V$  that maps  $e_t$  to  $s_j - s_i$  when  $e_t$  is the edge  $(s_i, s_j)$ .

To follow the analogy with classical signal processing, we want to derive tools to describe and study the properties of a graph signal. A first notion that we can express is the notion of variation of a signal among its domain. The gradient of a signal over an edge  $e = (i, j)$  is defined as the difference of the signal values at the extremities of the edge, following the orientation of the graph.

$$\text{grad}_e(s) = s(j) - s(i) \quad (1)$$

We naturally extend this to the linear mapping from  $\mathbf{R}^n$  to  $\mathbf{R}^p$  that maps a signal to the vector of gradients along each edge. We denote  $\nabla$  its matrix expressed in the bases  $V$  and  $E$ , such that

$$\nabla \cdot s = \begin{bmatrix} \text{grad}_{e_1}(s) \\ \text{grad}_{e_2}(s) \\ \vdots \\ \text{grad}_{e_p}(s) \end{bmatrix}$$



It is worth noting that this operator  $\nabla$  is nothing but the transposed incidence matrix of the graph.

Now that we have defined the gradient of the signal along its edges, we can express a notion of local variation at a node. The tool that we derive is the *graph Laplacian*. To pursue the analogy with classical vector calculus, the Laplacian of the signal at a node  $v$  is the divergence of the gradient through this point. Said differently, in our setting, it is the “oriented sum” of the variations of the signal from this point toward each direction. Once again, the graph’s orientation is followed.

$$\text{laplacian}|_v(s) = \text{div}|_v(\nabla \cdot s) = \sum_{e \text{ enter } v} \text{grad}|_e(s) - \sum_{e \text{ exit } v} \text{grad}|_e(s) \quad (2)$$

This nodewise operation extends to a linear mapping from  $\mathbf{R}^n$  (the signal) to  $\mathbf{R}^n$  (the Laplacian of the signal at each node of the graph). From equation (2), we see that computing the divergence of the gradient over the edges is equivalent to applying the incidence matrix to the gradient field  $\nabla \cdot s$ . This incidence matrix equals  $\nabla^\top$ . This is consistent with the classical calculus analogy where the divergence operator is the transpose of the gradient operator. We can thus express a Laplacian operator  $L$  of the form  $L = \nabla^\top \nabla$  such that

$$L \cdot s = (\nabla^\top \nabla) \cdot s = \nabla^\top (\nabla \cdot s) = \begin{bmatrix} \text{laplacian}|_{v_1}(s) \\ \text{laplacian}|_{v_2}(s) \\ \vdots \\ \text{laplacian}|_{v_n}(s) \end{bmatrix}$$

Hence, the effect of the orientation of the graph cancels out because of the factorisation  $\nabla^\top \nabla$  and plays no role in the definition of the Laplacian operator.  $L$  can thus also be defined for non-oriented graphs: injecting equation (1) into equation (2), it follows that  $L$  satisfies the following relations, independent of orientation:

$$(L \cdot s)|_{v_i} = \sum_{v_j \text{ connected to } v_i} (s(i) - s(j)) \quad L = D - A$$

Where  $D$  is the diagonal matrix whose entries are the degree of each node, and  $A$  is the aforementioned adjacency matrix. This result shows that the Laplacian matrix encodes structural properties of the graph. It also fully characterizes the graph, up to a reordering of its nodes (indeed those definitions initially

depended upon the choice of the standard basis  $V = \{v_1, \dots, v_n\}$  of  $\mathbf{R}^n$ ).

We can provide a similar formulation for weighted graphs. We will just weight the gradient of the signal along an edge by the weight of this edge. Intuitively this expresses that two nodes linked together by a strong edge are heavily related, and thus a variation of the signal between those nodes should be more significant than the same variation along a weaker edge. The gradient operator is therefore expressed as  $W \times \nabla$  and we can derive the following similar formula for the weighted Laplacian matrix, where  $D$  is the diagonal matrix of the weighted degrees.

$$L = \nabla^\top (W \nabla) = D - W \quad (3)$$

### Spectral Analysis of the Graph Laplacian

We have derived an operator that solely depends on the structure of the graph, and quantifies the variation of a signal on this graph. Indeed, given a signal  $s$ , the Laplacian matrix can be used to express the *Dirichlet energy*  $E(s)$  of the signal:

$$E(s) \stackrel{\text{def}}{=} \frac{1}{2} \sum_{u,v} w_{u,v} (s(u) - s(v))^2 = s^\top L s$$

The Dirichlet energy quantifies how much the signal varies along each edge, taking into account the weight of each edge (*i.e.* how strongly the two nodes are related). A signal whose energy is low can be seen as a signal whose variations are *smooth* with respect to the structure given by the edges: a strong connection between two nodes leads to a similar value of the signal on both extremities. In the other hand, high energy, means that some strongly connected nodes have a significantly different value, hence some notion of abrupt variation.

Equation (3) also shows that the Laplacian matrix is real and symmetric, and thus admits a nice diagonal decomposition in a basis of orthogonal eigenvectors.

$$L = \chi \Lambda \chi^\top$$

Where  $\Lambda = \text{Diag}(\lambda_1, \dots, \lambda_n)$  is the diagonal matrix whose entries are the eigenvalues of  $L$  and  $\chi$  is the matrix of the corresponding eigenvector basis  $(v_1, \dots, v_n)$ . We will assume that  $\lambda_1 \leq \lambda_2 \leq \dots \leq \lambda_n$ . Observe that since  $L$  can also be written as  $L = \nabla^\top \nabla$ , it is a semi-positive matrix, thus its eigenvalues are non-negative. Also note that since each row of  $L$  sums to 0 (see equation (3)), 0 is an eigenvalue of  $L$ , and thus we have  $\lambda_1 = 0$ .

Because the  $v_i$ 's are vectors of  $\mathbf{R}^n$ , they correspond to signals on the graph. We will call them the (*eigen-*)modes of the graph. The analogy with the notion of mode that we already knew in physics (those of a vibrating membrane for example) can be made because both are solutions of a Dirichlet problem  $Lx = \lambda x$ . Using the eigenvector property of  $v_i$ , we have:

$$E(v_i) = v_i^\top L v_i = v_i^\top (\lambda_i v_i) = \lambda_i \|v_i\|^2$$

Therefore, the energy of a normalized eigenvector only depends on the associated eigenvalue. This gives an intuitive idea behind the ordering of the eigenvalues: low eigenvalues correspond to modes with small energy (and thus smooth variations: the analogue of low frequency signals for time series), while high eigenvalues lead to mode with high energy (and thus high variations — high frequency). This phenomenon can be observed in figure 7.

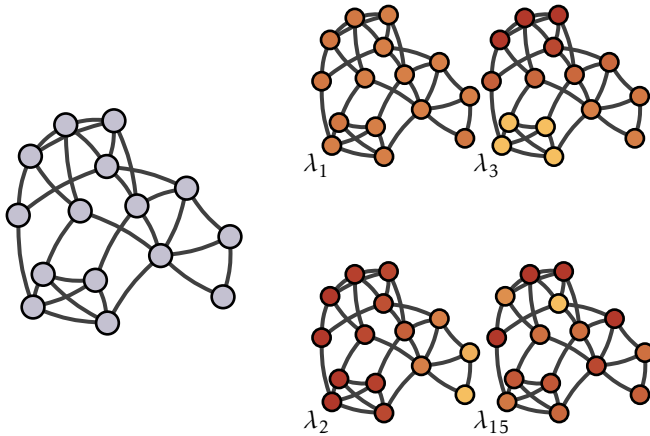


**Figure 7:** A graph, and some of the eigenvectors of its laplacian matrix. Note that the signal associated with  $\lambda_1$  (the zero eigenvalue) is the constant signal across the graph. Also observe that higher eigenvalues are associated with signal presenting more abrupt variations.

Since we have a basis of signals, we can decompose any signal  $s$  into his representation  $h$  on the basis represented by  $\chi$ , such that

$$s = \chi h = h_1 v_1 + h_2 v_2 + h_3 v_3 + \dots + h_{15} v_{15}$$

This is what is referred to as the *Fourier Transform* for graphs signals. We can thus decompose any graph signal into a sum of the modes of the graph, and the coefficients of this decomposition contain the spectral information of the signal. Because  $\chi$  is orthogonal, this decomposition can be obtained through

$$h = \chi^\top s$$

## 2.2. Optimal Transport of Smooth Graph Signals

Optimal transportation theory provides tools to endow *probability spaces* with a metric. Among those tools are the *Wasserstein distance* between probability measures (see appendix A for an in-depth introduction). Up to now, we have only been working with graphs, that are discrete objects but no distributions. An idea introduced in Dong et al.<sup>17</sup> is that a graph comes with a family of signals that are somehow natural on it: *smooth* signals. The core idea of the paper is that we can define a meaningful distribution of such smooth signals over the graph, and exploit the power of optimal transport tools on them. With the framework that we have introduced in the previous section, this corresponds to signals whose spectral mass is mainly concentrated around modes of low frequency.

<sup>17</sup> Dong et al. (2016)

The authors describe the following distribution of smooth signals over the graph. A random smooth signal should be such that the coefficient  $h_i$  associated to the eigenvector of  $v_i$  in its spectral decomposition follows  $\mathcal{N}\left(0, \frac{1}{\lambda_i}\right)$ . Said differently: the higher the eigenvalue of a mode, the more its spectral mass will be squeezed toward 0. Such a distribution will thus favour the low frequency modes and naturally lead to a class of smooth signals over the graph. The vector  $h$  thus follows a multivariate distribution  $\mathcal{N}\left(0, \Lambda^{-1}\right)$ . Using the fact that a signal  $s$  and its decomposition  $h$  are linked through  $s = \chi h$ , this gives a distribution of signals that can be expressed as the following multivariate distribution:

$$\mathcal{N}\left(0, \underbrace{\chi \Lambda^{-1} \chi^\top}_{L^{-1}}\right)$$

For correctness sake, we should mention that the Laplacian matrix is not truly invertible (recall that 0 is one of their eigenvalues), and thus the inverses mentioned earlier should rather be written as  $L^\dagger$ , where  $\cdot^\dagger$  denotes the pseudo-inverse of the matrix.

The authors of Maretic et al.<sup>18</sup> use this link between a graph and a distribution of signals to use the framework of optimal transport. Since the objects manipulated have gone from the space of graphs to a space of distributions, they propose to use an optimal transport measure (the Wasserstein distance) to the problem of comparing two graphs. This idea is summed up in figure 8.

<sup>18</sup> Maretic et al. (2019)

We thus need to compute an optimal transport distance between those measures. One of the drawbacks of today's optimal transport theory is its lack of tractable numerical schemes, espe-

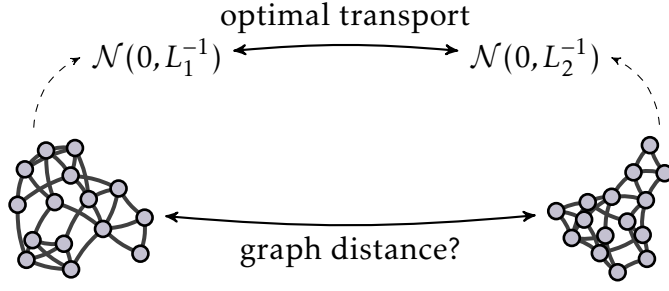


**Figure 8:** Using the optimal transport framework to compare two graphs: process used in Maretic et al.<sup>18</sup>

cially for high dimensional distributions. Fortunately, the distributions considered here (multivariate Gaussians) enjoy quite a few good properties and the authors of<sup>18</sup> use an explicit formulation for the 2-Wasserstein distance between two multivariate Gaussian distributions (also referred to as the Bures-Wasserstein distance<sup>19</sup>): if  $\nu_1 = \mathcal{N}(0, \Sigma_1)$  and  $\nu_2 = \mathcal{N}(0, \Sigma_2)$ .

<sup>18</sup> Maretic et al. (2019)

<sup>19</sup> Bhatia et al. (2019)

$$W_2^2(\nu_1, \nu_2) = \text{tr } \Sigma_1 + \text{tr } \Sigma_2 - 2 \text{tr } \sqrt{\Sigma_1^{1/2} \Sigma_2 \Sigma_1^{1/2}}$$

The square roots are well defined in our case since the Laplacian matrix — and thus their (pseudo-)inverses — are positive semi-definite.

Note that for this approach to make sense, the graphs must have the same number of nodes and they also should be aligned. This means that the ordering of the nodes of each graph should be meaningfully comparable in both graphs: for instance if one was to compare some networks associated to the economy of two countries, the capital of each country should correspond to the same node  $\nu_i$  in both graphs. The article Maretic et al.<sup>18</sup> dwells upon the issue of finding a good graph alignment, but we are not concerned by this since the networks that we will compare are issued using known brain atlases and we have thus enough prior knowledge of the networks to align them beforehand.

### 2.3. Wasserstein Distance on our Connectivity Matrices

At this point, we decided to try using the 2-Wasserstein distance on the dataset at our disposal. We wanted to observe the differences between controls and patients. A latent idea was that we could be able to classify a new subject from its connectome using the developed technique. This was backed up by studies having brought out significative connectivity difference between the control and the depressive cohorts. I thus implemented the distance introduced in Maretic et al.<sup>18</sup> that I discussed in the previous section. The hope was that the known structural differences<sup>4</sup>

<sup>18</sup> Maretic et al. (2019)

<sup>4</sup> Coloigner et al. (2018)

between the two cohorts would be captured by the transportation distance between graphs.

The approach I first chose is to compute a pairwise distance between each subject and each control. I aggregated those distance into an average distance to the control cohort for each subject. Our intuition was that, because of the connectivity change in specific networks related to the disease, the average distance between a control and the cohort of other controls would be smaller than the average distance between a patient and the cohort of control. In figure 9, I represented the distribution of average distances to the control group from either the control group or the patient group. We expected to see a shift in the distributions, reflecting the greater homogeneity inside the control group.

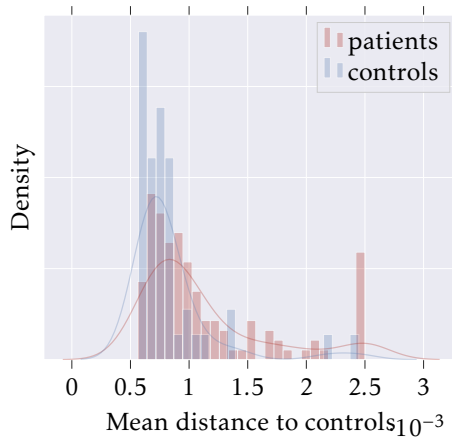


**Figure 9:** Pure Wasserstein distance to controls, the spike at the right corresponds to distances that were clipped to  $2.5 \cdot 10^{-2}$ , in order to keep a readable scale.

Although it captures the greater homogeneity among controls, the distance does not really discriminates between both groups. Even though we endorse the matrix space with a meaningful geometry, its high-dimensionality might still make it hard to analyze, the same way k-Nearest-Neighbours classifiers tend to struggle with high dimensionality data.

## 2.4. Barycenters of Gaussian distributions

An idea that I proposed to enhance results is to have a notion of barycenters of connectomes. This approach emerges naturally since we are willing to compare cohorts: being able to compute a mean connectome of a control group to which we compare individual subjects instead of averaging individual distances to subjects might provide better results than the previous approach. A geometric intuition of why this could enhance our results is provided in figure 10.

The notion of barycenter (or centroid) is well defined in euclidean spaces. It finds a natural generalization in metric spaces

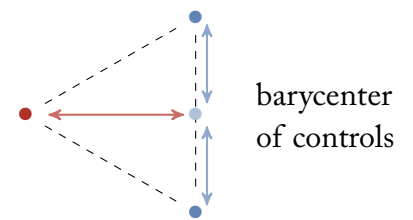


**Figure 10:** Geometric intuition of why to use barycenters in our study. Even though all subjects are roughly equidistant and thus hard to distinguish simply by computing the pairwise distances (in some arbitrary metric space), the controls (blue) are closer to their barycenter than the patient (red), and computing individual distances to the barycenter allows to classify more reliably.

with the formulation of the Fréchet mean. This gives, for instance, a natural way to define the geometric mean as a centroid: via the Fréchet mean for the hyperbolic distance.

As detailed earlier, we have embedded connectivity graphs into a probability space endowed with the Wasserstein metric. The formulation of the Fréchet mean  $\bar{\mu}$  of a collection of measures  $(\mu_1, \dots, \mu_k)$  in this space (which we will also call a *Wasserstein barycenter*) is as follows:

$$\bar{\mu} = \arg \min_{\mu} \sum_{i=1}^k \lambda_i W_2^2(\mu, \mu_i) \quad \text{where } (\lambda_1, \dots, \lambda_k) \text{ are weights}$$

Computation of such barycenters in the theory of optimal transport often relies on samples of the distributions. See for instance Peyré, Cuturi, et al.<sup>20</sup> for a review of numerical schemes behind this optimisation problem. Unfortunately, our distributions of interest are not described by samples but rather by their covariance matrix, which is convenient because sampling such high dimensionality distributions is expensive. Fortunately, multivariate Gaussians are easy to work with, and we will be able to use results of Álvarez-Esteban et al.<sup>21</sup> that gives an interesting and computationally fecund characterization of the Wasserstein barycenter, which happens to be the fixed point of a certain application:

$$\bar{\mu} = G(\bar{\mu})$$

$G$  is defined as the function mapping a distribution  $\mu$  to the distribution followed by  $\sum_{i=1}^k \lambda_i T_i(X)$  where  $X \sim \mu$  and  $T_i$  is the transport map sending  $\mu$  to  $\mu_i$ . One can get the intuition of this result as follows: the barycenter is the measure that is stabilized when geodesically moved toward each of the  $\mu_i$ . Note that the subtlety here is that the distributions followed by each of the  $T_i(X)$  are not independent of each other because the one and only random variable  $X$  is transported in each term. We will apply this result to our multivariate normal distributions.

A known result is the expression of  $T_i$  when we transport a Gaussian toward another Gaussian distribution, see *e.g.* Bhatia, Jain, and Lim<sup>19</sup>. If  $\mu = \mathcal{N}(0, \Sigma)$  and  $\nu_i = \mathcal{N}(0, \Sigma_i)$ ,

$$T_i(x) = \Sigma^{-1/2} \left( \sqrt{\Sigma^{1/2} \Sigma_i \Sigma^{1/2}} \right) \Sigma^{-1/2} x \quad (4)$$

We denote  $A_i$  the matrix in front of  $x$  in the above expression. Applying the map  $G$  to the Gaussian measure  $\mu = \mathcal{N}(0, \Sigma)$  when each  $\nu_i$  is of the form  $\mathcal{N}(0, \Sigma_i)$  yields that  $G(\mu)$  is the distribution

<sup>20</sup> Peyré et al. (2019)

<sup>21</sup> Álvarez-Esteban et al. (2015)

<sup>19</sup> Bhatia et al. (2019)



of a sum of affine transformations of Gaussians random variables, whose mean is 0, and whose covariance matrix can be expressed as:

$$\begin{aligned}
(\lambda_1 A_1 \quad \dots \quad \lambda_k A_k) \begin{pmatrix} \Sigma & \dots & \Sigma \\ \vdots & \ddots & \vdots \\ \Sigma & \dots & \Sigma \end{pmatrix} \begin{pmatrix} \lambda_1 A_1 \\ \vdots \\ \lambda_k A_k \end{pmatrix} &= \sum_{i,j}^k (\lambda_i A_i) \Sigma (\lambda_j A_j) \\
&= \sum_{i,j}^k \lambda_i \lambda_j \left( \Sigma^{-1/2} \sqrt{\Sigma^{1/2} \Sigma_i \Sigma^{1/2}} \Sigma^{-1/2} \right) \Sigma \left( \Sigma^{-1/2} \sqrt{\Sigma^{1/2} \Sigma_j \Sigma^{1/2}} \Sigma^{-1/2} \right) \\
&= \Sigma^{-1/2} \left( \sum_{i=1}^k \lambda_i \sqrt{\Sigma^{1/2} \Sigma_i \Sigma^{1/2}} \right)^2 \Sigma^{-1/2}
\end{aligned}$$

The authors of<sup>21</sup> show that — under some mild hypothesis — this function  $G$  gives a natural iteration scheme  $\mu_{n+1} = G(\mu_n)$  that converges to the unique fixed point of  $G$ , which is the desired barycenter. If we denote  $\mu^{(n)} = \mathcal{N}(0, \Sigma^{(n)})$ , it provides the following iteration scheme that converges toward the covariance of the barycenter:

<sup>21</sup> Álvarez-Esteban et al. (2015)

$$\Sigma^{(n+1)} = \Sigma^{(n)-1/2} \left( \sum_{i=1}^k \lambda_i \sqrt{\Sigma^{(n)1/2} \Sigma_i \Sigma^{(n)1/2}} \right)^2 \Sigma^{(n)-1/2}$$

Figure 11 shows the result of this iterative scheme to compute the barycenter of four two-dimensional Gaussians.

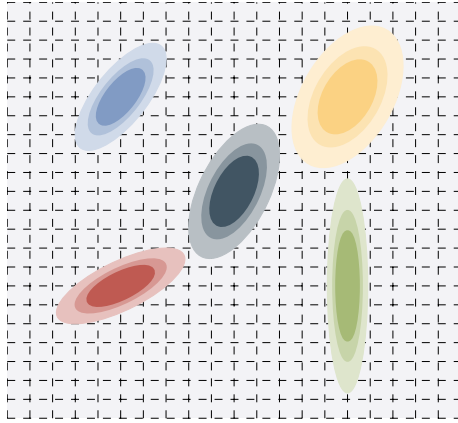


**Figure 11:** Barycenter of 2D Gaussians computed using the iterative scheme. The barycenter is the darkest distribution, in the middle. Observe that the barycenter have benefited from characteristics of all measures, while avoiding overrepresentation of individual variability, such as the squeezing of the green distribution.

## 2.5. Barycenters for Connectivity Analysis

The idea at this point was that we could continue to compare connectomes in the probability space introduced earlier, but instead of individually comparing subjects to each control, we can

now start by computing a barycenter of the group of interest and then compare each subject to this barycenter. Not only this increases the speed of comparing a new subject to the control cohort since only one distance needs to be computed, but this also leverages that we are comparing a subject to the relevant features common across a whole cohort, thus avoiding too much emphasis put on individual variability. In figure 12 I show the barycenter computed from the full controls cohort.

To assess the utility of barycenter, I devised the experiment shown in figure 13. I repeatedly split the control cohort into two, used one part of the controls to compute a barycenter, and computed the distance between the other controls and the patients to the barycenter.

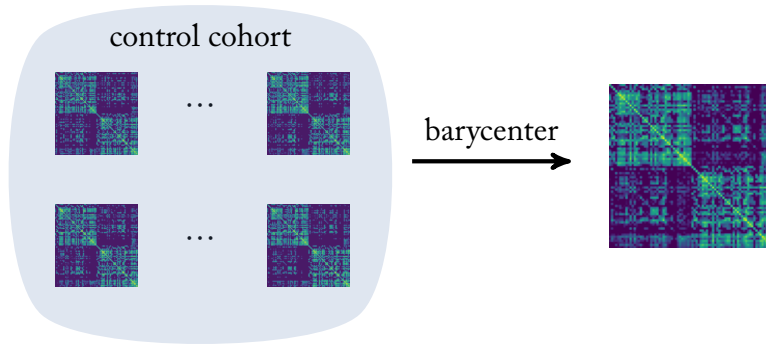


**Figure 12:** Barycenter computation. Note that we compute the barycenter in a probability space, and that the shown connectivity matrix only approximately corresponds to a true network.

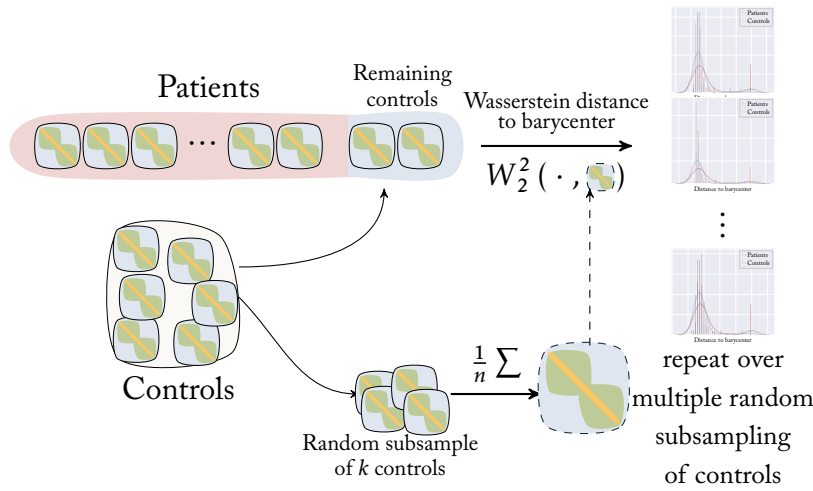


**Figure 13:** Barycenter folding tests. Note that the  $\frac{1}{n} \sum$  arrow denotes the computation of the Wasserstein barycenter.

Once again, the results (see figure 14) were not significantly more satisfying than those obtained through the first method. The expected shift in the distributions, although existing because of the greater homogeneity in the control group, is not significant, and only a handful of patients are indeed discriminated by those distance-based methods.

I conducted further experiments, either by increasing the sparsity of the networks, or by splitting the connectome into hemi-

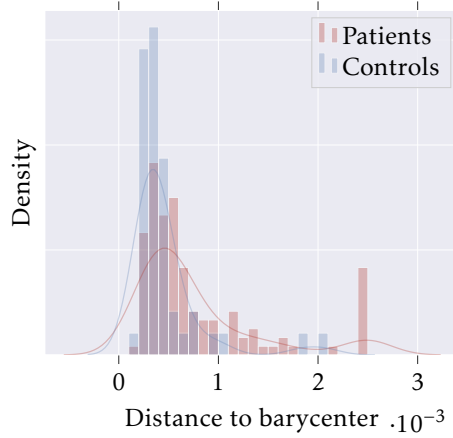


**Figure 14:** Distances to the control barycenter aggregated from the folds of the experiment presented in figure 13.

spheric subnetworks to exploit some properties of the distance described in Maretic et al.<sup>18</sup>, but none of those yielded better results.

<sup>18</sup> Maretic et al. (2019)

### 3. Graph Curvature

I investigated another marker that could be used to capture properties of the network. There is often a duality between *mesh processing* and graph analysis. Indeed, the tools introduced in section 2 in the context of graph signal processing, such as the graph Laplacian, are also defined and used in mesh processing. The intuition behind this is that shapes can often be summarized through their combinatorial structure, and thus through an adjacency graph. Ollivier-Ricci curvature is another of those common tools, whose intuition first come from geometric objects, but can provide insight on the structure of the graph. This tool starts to be used for complex network analysis, such as in Ni et al.<sup>22</sup> or Sia, Jonckheere, and Bogdan<sup>23</sup>, and even in the context of neurosciences like in Farooq et al.<sup>24</sup> I will introduce this tool, the intuition backing it as well as its theoretical foundations. I will also present novel ideas to adapt this tool in the context of our study.

<sup>22</sup> Ni et al. (2015)

<sup>23</sup> Sia et al. (2019)

<sup>24</sup> Farooq et al. (2019)

#### 3.1. From Riemannian manifolds to networks

Curvature is usually defined on geometric objects, as we will first see. I will then present how a notion of curvature can be computed on combinatorial objects (graphs in our context), and convey information on the structure of the object.

##### Ricci curvature on manifolds

A *manifold* can be roughly defined as a space that locally coincides with a Euclidean space. More precisely, a  $n$ -manifold is a set

$\mathcal{M} \subset \mathbf{R}^d$  such that for each point  $x$  of  $\mathcal{M}$ , there exist an affine subspace of  $\mathbf{R}^d$  of dimension  $n$  that coincides with  $x$  at first order. This space is called the tangent space of  $\mathcal{M}$  at  $x$ . An example of such set is a sphere embedded in  $\mathbf{R}^3$ . Its local similarity with a Euclidean space is responsible for the phenomenon that makes the Earth hardly distinguishable from a plane at first order, at the human scale.

Thinking about *curvature* is trying to quantify how much the manifold differs from a Euclidean space at second order. Several notions of curvature coexist. I will briefly introduce the *sectional curvature* and the *Ricci curvature*, both defined in the setting of *Riemannian manifolds*.

A Riemannian manifold is a manifold  $\mathcal{M}$  equipped with a *Riemannian metric*. That is for every point  $x$  in  $\mathcal{M}$ , there exist an inner product defined in the tangent space of  $\mathcal{M}$  at  $x$ , inducing a norm in this tangent space. A *canonical* such Riemannian metric is the restriction of the Euclidean inner product to the tangent space. This is illustrated in figure 15 for a sphere.

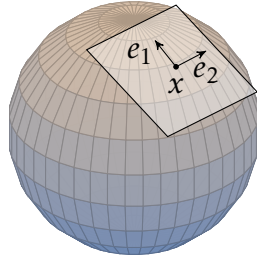


**Figure 15:** The sphere  $\mathcal{S}$  embedded in  $\mathbf{R}^3$  seen as a two dimensional Riemannian manifold. The tangent space of  $\mathcal{S}$  at point  $x$  is the affine space represented, and an orthogonal basis  $(e_1, e_2)$  of this space can be used to define the canonical inner product inside this tangent space.

Given a smooth curve  $\gamma$  on  $\mathcal{M}$  ( $t \mapsto \gamma(t) \in \mathcal{M}$ ), its derivative  $\frac{d\gamma}{dt}(t)$  is a vector of the tangent space of  $\mathcal{M}$  at  $\gamma(t)$ , whose length can thus be defined thanks to the norm induced on the tangent space. By integration along the curve, we can therefore define the length of the curve. The *geodesic distance* between two points of  $\mathcal{M}$  is the infimum of the length of a smooth curve joining the two said points. This induces a metric  $d$  on the manifold, such that  $d(x, y)$  is the geodesic distance between those two points.

Using some geometrical intuition, we can easily define the *parallel transport* of a tangent vector along a curve. This is illustrated in figure 16 where we transport the tangent vector  $w_x$  from  $x$  to  $y$  along  $v$ , giving the vector  $w_y$  tangent to the manifold at  $y$ . This can be used to assess the local discrepancy between a manifold and a Euclidean space. Indeed, in a pure Euclidean setting, parallel vectors are actually rigorously parallel, in the sense that following both vectors does not result in either convergence or divergence. In a Riemannian manifold, parallel vectors are defined to be as parallel as the space allows it, which can result in convergence or

divergence when following the geodesic they define.

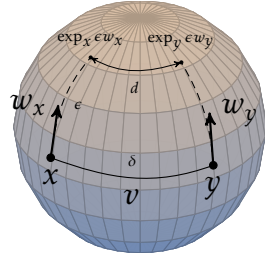


**Figure 16:** Parallel transport of  $w_x$  from  $x$  to  $y$  following  $v$ . The dotted lines represent the constant-speed geodesic starting from either  $x$  or  $y$  with initial speed given by the tangent vectors  $w_x$  and  $w_y$ , and running for a time  $\epsilon$ . The sectional curvature at  $x$  in direction  $w$  along  $v$  (denoted  $K(v, w_x)$ ) will be defined through the behaviour of  $d$  when  $\epsilon \rightarrow 0$  and  $\delta \rightarrow 0$ .

More formally, using the notations from figure 16, the sectional curvature in direction  $w_x$  along  $v$  (denoted  $K(v, w_x)$ ) is defined as a second order coefficient in the asymptotic behaviour of  $d(\exp_x \epsilon w_x, \exp_y \epsilon w_y)$ :

$$d(\exp_x \epsilon w_x, \exp_y \epsilon w_y)_{\epsilon, \delta \rightarrow 0} = \delta \left( 1 - \frac{\epsilon^2}{2} K(v, w_x) + \mathcal{O}((\delta + 1)\epsilon^2) \right)$$

This highlights that a positive sectional curvature leads to converging parallels (like on the above sphere), while a negative curvature leads to diverging parallels. This definition is dependant on both the direction  $v$  along which we transport and on the vector  $w_x$  that is transported. *Ricci curvature* is defined as the average of sectional curvature over all the directions  $w_x$  in the tangent space at  $x$ .

This can also be rephrased in term of asymptotic behaviour, in similar fashion to the definition of  $K$ . If we define  $\bar{d}$  to be the average of the distances  $d$  depicted in figure 16 for  $w_x$  describing the unit circle in the tangent space, we have

$$\bar{d}_{\epsilon, \delta \rightarrow 0} = \delta \left( 1 - \frac{\epsilon^2}{2N} \text{Ric}(v) + \mathcal{O}((\delta + 1)\epsilon^2) \right)$$

## Ollivier-Ricci Curvature in Metric Space

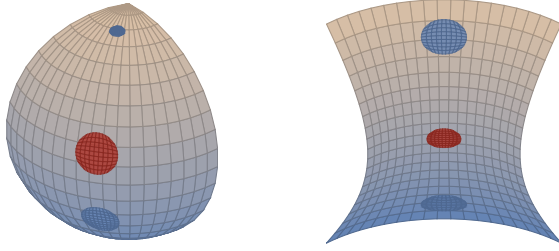
This previous definition of Ricci curvature is only valid in Riemannian manifolds. We would like to extend it to general metric spaces, such as graphs, while keeping the intuitions behind it. I will detail the approach formulated by Ollivier<sup>25</sup>. His approach finds its roots in theorems, formulated by Lott and Villani, as well as Sturm, linking optimal transport distances, Boltzmann entropy (denoted  $H$  in what follows) and Ricci curvature on (still) Riemannian manifolds.

<sup>25</sup> Ollivier (2009)

To understand the relationship between those notions, let us look at the following theorem, which has a very intuitive interpretation. If  $k$  is a lower bound for the Ricci curvature on the manifold  $\mathcal{M}$ ,  $\mu_0$  and  $\mu_1$  are measures defined on  $M$ , and  $(\mu_t)_{t \in ]0,1[}$  is the interpolation between those two measures (in the sense of the Wasserstein  $W_2$  metric, see appendix A for more details), we have<sup>26</sup>

$$H(\mu_{\frac{1}{2}}) \geq \frac{1}{2}(H(\mu_0) + H(\mu_1)) + \frac{k}{8}W_2^2(\mu_0, \mu_1) \quad (5)$$

If we remind, from information theory, that entropy basically accounts for the spread of the measure (entropy increases as the measure gets closer to being uniform), this theorem is actually saying that measures defined on a manifold tend to spread under positive curvature, while they are able to get shrunk while on negatively curved spaces. This can be observed in figure 17.



<sup>26</sup> Renesse et al. (2005)

**Figure 17:** Dilatation (left) and contraction (right) property of the entropy under positive (left) and negative (right) curvature. Blue areas represent measures of finite support on the manifold. The red measure in the center represents (both in the left and right cases) the interpolation (in the Wasserstein sense) between the two others.

Another property, that will get us closer to the definition of Ollivier-Ricci curvature is the following. If we define  $m_{r,x}$  to be the uniform measure on  $\mathcal{M}$  whose support is the circle of center  $x \in \mathcal{M}$  and of radius  $r$  (for the geodesic distance on  $\mathcal{M}$ ), one can show<sup>26</sup> that equation (5) under the condition  $\text{Ric}(\mathcal{M}) \geq k$  is equivalent to

$$W_1(m_{r,x}, m_{r,y}) \leq \left(1 - \frac{k}{2(n+2)}r^2 + o(r^2)\right)d(x, y) \quad (6)$$

<sup>26</sup> Renesse et al. (2005)

This last theorem is interesting, providing a link between a lower bound  $k$  of the curvature and the geodesic distance  $d$  on the manifold  $\mathcal{M}$ . It is the inspiration for the definition of a notion of curvature on metric spaces, removing the need for a Riemannian framework.

Hence, in a geodesic metric space  $(\mathcal{X}, d)$  equipped with a set of measures  $\{p_x \mid x \in \mathcal{X}\}$ , Ollivier<sup>25</sup> defined the *Ollivier-Ricci curvature*  $\kappa(x, y)$  of the geodesic linking  $x$  and  $y$  using the following equation:

<sup>25</sup> Ollivier (2009)

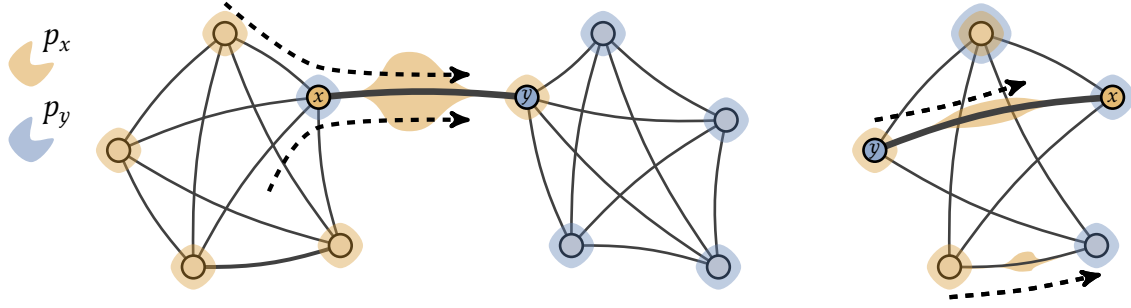


**Figure 18:** Intuition of Ollivier-Ricci curvature on graph.  $p_x$  and  $p_y$  are measures spread among the neighbourhoods of  $x$  and  $y$ . The curvature of the edge  $(x, y)$  depends on how  $p_x$  is transported to  $p_y$ . The bold  $(x, y)$  edge on the left has a negative curvature, because it connects two disjoint community and thus most of the mass of  $p_x$  has to be transported through this edge, causing the transportation distance to be at least  $d(x, y)$ . On the right, the edge has positive curvature, because it connects nodes from the same community and that share neighbours. There is less mass to move, and on shorter paths, so the total transportation distance is less than  $d(x, y)$ .

$$W_1(p_x, p_y) = (1 - \kappa(x, y))d(x, y) \quad (7)$$

The  $p_x$  here stands for a measure concentrated around  $x$ , which is similar to the  $m_{r,x}$  introduced earlier. One can notice the direct analogy between the definition (7) and equation (6).

A direct interpretation of a positive Ollivier-Ricci curvature between  $x$  and  $y$  is the following: if one wants to transport a mass spread around  $x$  toward a mass spread around  $y$ , the total cost is smaller than the geodesic distance between  $x$  and  $y$  (from equation (7)). That might be because two points on the neighbourhood of  $x$  and of  $y$  are closer than  $x$  and  $y$  for the geodesic distance. Typically on a graph, nodes  $x$  and  $y$  might share neighbours, or well-connected neighbour's. Conversely, a negative curvature shows that the best way to transport the mass between  $x$  and  $y$  might be to actually follow the geodesic between  $x$  and  $y$ . In the context of a graph, positive curvature tends to happen inside communities, while negative curvature appears for inter-community edges. This is highlighted in figure 18.

This provides a tool that can be used on graphs, as long as a geodesic distance can be defined on those. Indeed, 1-Wasserstein distance can easily be computed using dynamic programming. Some studies have provided good evidence that this can capture deep structural information about graphs<sup>27</sup>. Those intuitions are backed up by some theoretical results: for instance Bauer, Jost, and Liu<sup>28</sup> show a link with the spectrum of the Laplacian matrix of a graph, which is known to carry structural information as well.

<sup>27</sup> Ni et al. (2019)

<sup>28</sup> Bauer et al. (2011)



### 3.2. Ollivier-Ricci Curvature on Connectivity Graphs

My idea here, was to follow an approach used in structural connectivity analysis with some of the topological indicators mentioned in section 1 (see figure 4). A way to use those local metrics is to compute them for each node of each subject, and then, for each node, compare the distribution of metric behind the control group and the patient group for instance. Any significant difference would cause the node (and thus the corresponding brain area) to be considered of interest for the studied pathology. This is what is done in Coloigner et al.<sup>4</sup> for instance. I wanted to adopt a similar strategy, but using curvatures instead of the more “traditional” measures. It turned out that a recent paper<sup>24</sup> had already devised a similar method, with relative success.

<sup>4</sup> Coloigner et al. (2018)

<sup>24</sup> Farooq et al. (2019)

I described in the previous theoretical section, the only requirement to compute an Ollivier-Ricci curvature, is to have a metric space. In our context, this means being able to compute a distance between two nodes on the graph. The choice of Farooq et al.<sup>24</sup> was to consider shortest-paths in the connectivity graph, where the distance would simply be computed as the number of hops between two nodes. Even though accounting for the structure of the graph, choosing this notion of distance disregards the weights of connections, which is one of the drawbacks that we mentioned in section 1 and that we are trying to avoid.

<sup>24</sup> Farooq et al. (2019)

I made the choice to introduce another notion of distance, based on the *heat kernel* of the graph. The heat kernel is basically the solution to the diffusion equation at the surface of the graph, involving the graph laplacian derived in section 2.

$$\left( \frac{\partial}{\partial t} + L \right) f = 0$$

There is a direct analogy with the heat equation from physics. This equation describes the diffusion of what could be the electrochemical energy of a signal in the brain. As so, it is relevant to study brain networks<sup>29</sup>. Links can also be formulated between this equation and random walks on connectivity graphs. Those random walks have been studied with interest in Robinson<sup>30</sup> and Robinson et al.<sup>31</sup>

<sup>29</sup> Chung et al. (2016)

<sup>30</sup> Robinson (2012)

<sup>31</sup> Robinson et al. (2014)

A solution of this equation is  $f : t \mapsto e^{-tL} f_0$ . The matrix  $k_t = e^{-tL}$  is called the heat kernel of the graph, and each of its entries  $k_t(x, y)$  represents the amount of heat initially in  $x$  having reached  $y$  at time  $t$ . As a kernel, it defines a distance between nodes of the graph

$$d_t(x, y) = k_t(x, x) + k_t(y, y) - 2k_t(x, y)$$

This distance, for well chosen  $t$ , takes into account the combinatorial structure of the graph, as well as the strengths of the connections, as shown in figure 19. This makes it more suited than the “shortest number of hops” distance. Now that a distance is defined between nodes, we can compute the curvatures of each connection.

Looking at connections having significative curvature differences between controls and patients yields more connections of interest than the methods based upon classic topological markers (see figure 20, where we performed a similar analysis than in Coloigner et al.<sup>4</sup>). This is both consistent with the claims of Farooq et al.<sup>24</sup>, and with the intuition that curvature, along with the heat kernel distance, is locally sensitive to the global topology of the graph, and thus a wider part of the networks finds its curvature affected by slight changes between the control cohort and the patients.

<sup>4</sup> Coloigner et al. (2018)

<sup>24</sup> Farooq et al. (2019)

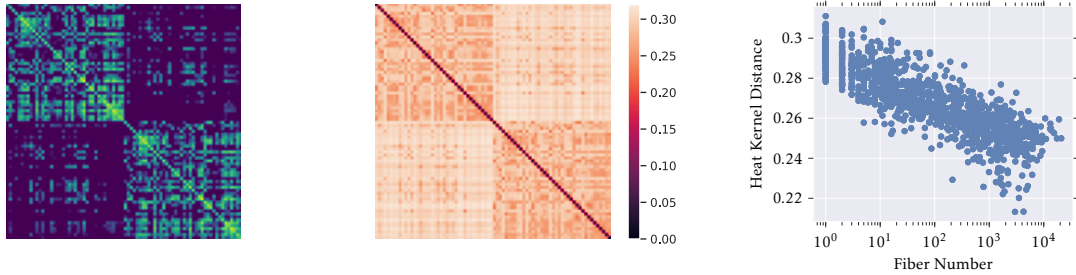


**Figure 19:** Heat Kernel distance computed on a connectivity matrix. Left: original connectivity matrix. Middle: heat kernel distance matrix. Right: each point represents a fiber connection (*i.e.* an entry of the original matrix), the  $x$  axis represents the strength of the anatomical connection, while the  $y$  axis is the heat kernel distance between each extremities of the connection.

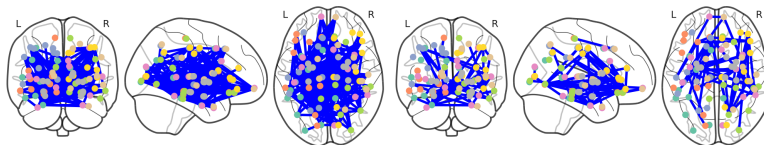


**Figure 20:** Left: connections with significative curvature difference between controls and patients. Right: connections with significative fiber number differences between controls and patients.

## Conclusion

I have proposed to use a distance between graphs introduced recently in Maretic et al.<sup>18</sup> I have also extended this distance by the use of barycenter computations. Having tried both approaches on

<sup>18</sup> Maretic et al. (2019)

the dataset at my disposal, it seemed that the computed distances and barycenters were able to capture and reflect some of the structural information of the connectomes. Yet, the distance was not subtle enough to really discriminate the two groups, which mitigate its use for further studies in this context. I think that the notion of barycenter for connectomes that I introduced could still prove useful, thanks to its ability to leverage structural information from a whole cohort. It would be of interest to do further experiments with it to better understand what it could yield, maybe with toy graphs. Another point that I have not fully exploited is the knowledge of the transport map associated with the Wasserstein distance.

I also studied Ollivier-Ricci curvature and its potential application to connectome comparison. I proposed a framework to use it in the setting of structural connectivity data that is novel from how it had already been used. It should circumvent some of the drawbacks of topological markers that we discussed in section 1 and that are still present in the recent uses of Ollivier-Ricci curvature for connectivity analysis<sup>24</sup>. I am still evaluating and comparing this approach to prior works. There are also techniques exploiting the Ollivier-Ricci curvature that are worth exploring, especially for connectome comparison. Among others lie the Ricci flow, that has been used with success for (non-biologic) complex networks, see for instance Weber, Jost, and Saucan<sup>32</sup> or Ni et al.<sup>27</sup>

<sup>24</sup> Farooq et al. (2019)

<sup>32</sup> Weber et al. (2016)

<sup>27</sup> Ni et al. (2019)

## A. Introduction on Optimal Transport

The history of optimal transport formulations can be traced back to Gaspard Monge's *Mémoire sur la théorie des déblais et des remblais* (1781). In this document, he studied how to move masses of sand or soil from one place to another. The main motivation of this *Mémoire* being that a cost is naturally associated to the act of moving a mass particle from one place to another, and it is of particular interest to seek the optimal way of moving a global quantity of mass from one place to another, that should require the lowest amount of effort possible.

### Monge's formalism

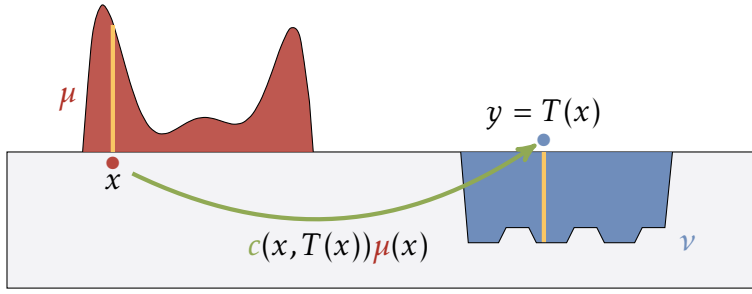


**Figure 21:** Earth mover problem. We want to fill the blue hole (the *déblai*, which is also called the *target distribution*  $\nu$ ) using the red matter (the *remblai*, which is also called the *source distribution*  $\mu$ ).  $T$  represents the transport map, describing a way to send particles from the source distribution to the target distribution.  $c(x, T(x))$  is the cost of moving from  $x$  to  $T(x)$

We work in a space  $\Omega$ . We consider two probability measures  $\mu$  and  $\nu$  on  $\Omega$ , respectively the *source* and the *target* distribution. We also consider a cost function  $c : \Omega \times \Omega \rightarrow \mathbf{R}$ . If  $\Omega$  is some Euclidean space,  $c$  can, for instance, be the Euclidean distance induced in it. Monge's problem is formulated as follows:

$$\begin{aligned} \min_{T: \Omega \rightarrow \Omega} \int_{\Omega} c(x, T(x)) d\mu(x) \\ \text{s.t. } \forall A \in \mathcal{P}(\Omega), \nu(A) = \mu(T^{-1}(A)) \end{aligned}$$

The function  $T$  is called a transport map. It carries information about the displacement of each elementary unit of probability: the mass located in  $x$  is moved toward  $T(x)$ . The function  $c$  thus allows quantifying the cost of moving one elementary unit of mass. We want to minimize the average distance travelled by mass units during the optimal transport. The condition under which the optimization is performed ensures that all the mass of  $\mu$  has been transported toward the distribution  $\nu$ . Those concepts are introduced in figure 21.

The issue with such a formulation of an optimal transport problem is that it does not handle discrete probability measures.

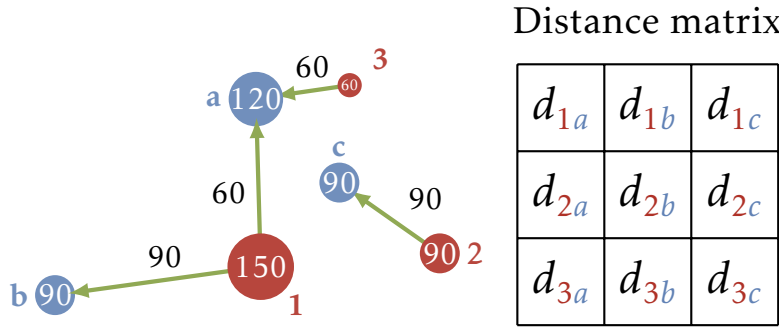


**Figure 22:** A discrete Kantorovich problem. The red distribution is still the source distribution and the blue the target one. Now that we work in a discrete setting, the cost function has been replaced by a distance matrix, expressing the pairwise costs of moving from one atom of the source distribution to an atom of the target distribution.

Indeed, if  $\mu$  has a Dirac impulse bigger than every Dirac impulse of  $\nu$ , then the transport map cannot be built: we are only performing displacements of mass and not any actual allocation of mass. For example in figure 21, we are not allowed to split any of the transported yellow units.

### Kantorovich's formalism

Kantorovich came up with an alternative formulation for the optimal transport problem, that aims at handling discrete distributions. Kantorovich's idea was to change the function  $T : \Omega \rightarrow \Omega$  into a probability  $P$  on the product space  $\Omega \times \Omega$  called the *transport map*. The probability  $P(x, y)$  describes how much of the mass in  $x$  is moved toward  $y$ . If we denote  $D$  the distance matrix encoding the costs of the problem, we obtain the following formulation in the discrete case:

$$\begin{aligned} \min_P \quad & \langle P, D \rangle = \sum_i \sum_j p_{ij} d_{ij} \\ \text{s.t.} \quad & \begin{cases} \forall i \quad \sum_j p_{ij} = \mu_i \\ \forall j \quad \sum_i p_{ij} = \nu_j \end{cases} \end{aligned}$$

The two conditions encode the fact that we aim to move all the mass of  $\mu$  toward all the mass of  $\nu$ . In the problem represented in figure 22, Monge's formulation forbids to split the mass of size 150 into two separate masses, and the problem is not feasible. Yet, Kantorovich's formulation allows this: as shown in figure 22, the mass of 150 is split into a mass of 90 and a mass of 60, both sent to different places.

This is clearly a *linear program*, for which efficient solvers are still under extensive study; Peyré, Cuturi, et al.<sup>20</sup> provides a detailed overview of many numerical aspects of this problem.

<sup>20</sup> Peyré et al. (2019)

### Continuous Kantorovich's formulation

In the continuous setting, we introduce the following set of joint probabilities, which encodes the analogue of the two conditions

in the discrete case, making sure that  $\mu$  has been fully transported to  $\nu$ .

$$\Pi(\mu, \nu) = \{P \in \mathcal{P}(\Omega \times \Omega) \mid \forall A, B \in \Omega, P(A \times \Omega) = \mu(A), P(\Omega \times B) = \nu(B)\}$$

We can rephrase the definition of  $\Pi(\mu, \nu)$  as being the set of probability measures on  $\Omega \times \Omega$  with marginals  $\mu$  and  $\nu$ . We consider once again a cost function  $c$  as in Monge's problem. Kantorovich's formulation now becomes the following optimization problem, where  $X \sim \mu$  and  $Y \sim \nu$ :

$$\inf_{P \in \Pi(\mu, \nu)} \mathbb{E}_P[c(X, Y)] = \iint_{\Omega \times \Omega} c(x, y) P(x, y) dx dy$$

### Existence of solutions to Kantorovich's problems

One can wonder, in light of what happened for Monge's problems, whether solutions of Kantorovich's problem as formulated above exist. A rich literature exists on this topic. For instance, in the case of measures on the  $\mathbf{R}^n$  space, with absolutely continuous measures  $\mu$  and  $\nu$  with respect to the Lebesgue measure, the existence (and uniqueness) of solutions will only depend on the properties of the cost function. If we consider the cost function  $c_p(x, y) = \|x - y\|^p$ , then we have the following discussion:

- $p > 1$ : the strict convexity of  $c_p$  ensures that there is a unique solution to the Kantorovich problem
- $p = 1$ : here we can obtain the existence of a minimizer for the Kantorovich, but we won't have the unicity of the solution
- $p < 1$ : in general, there will not exist solutions to the problem

More generally the existence of minimizers, as well as their uniqueness depends heavily on the structure of the space we consider, and the properties of both the measures and the cost function. A comprehensive study of those properties can be found in Villani<sup>33</sup>.

<sup>33</sup> Villani (2003)

### Wasserstein distance.

Having formulated this optimization problem allows us to define a distance between probability measures. Given a probability space  $\Omega$ , a cost function  $c : \Omega \times \Omega \rightarrow \mathbf{R}_+$  and two probability

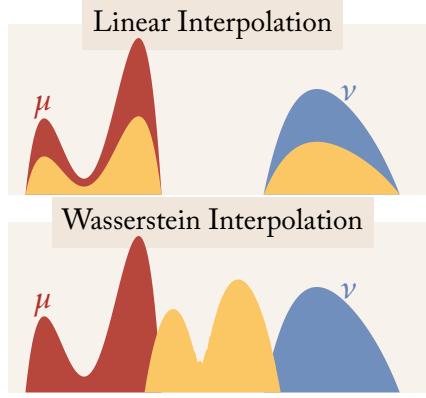


**Figure 23:** Two interpolations (in yellow) between  $\mu$  and  $\nu$ . Left: linear interpolation, defined as  $(\mu + \nu)/2$  (or equivalently as  $\arg \min_{\eta} l_2^2(\mu, \eta) + l_2^2(\nu, \eta)$ , where  $l_2^2$  is the squared difference between shapes) . Right: Wasserstein interpolation, defined as  $\arg \min_{\eta} W_2^2(\mu, \eta) + W_2^2(\nu, \eta)$

measures  $\mu$  and  $\nu$  in  $\mathcal{P}(\Omega)$ , the **p-Wasserstein-distance** between  $\mu$  and  $\nu$  is defined as

$$W_p(\mu, \nu) = \left( \inf_{P \in \Pi(\mu, \nu)} \iint_{\Omega \times \Omega} c(x, y)^p P(x, y) \, dx \, dy \right)^{1/p}$$

### Wasserstein barycenters.

This notion of distance allows to compute barycenters between probability distributions, and obtain results that are way more natural than barycenters obtained with respect to other norms, like the  $l_2$  norm for instance. Figure 23 presents a barycenter obtained under Wasserstein-distance and a linear interpolation (the two averaged distributions being the blue and the red one, and the yellow shape being the barycenter. What emerges from those two interpolations is that the Wasserstein distance seems particularly well suited to manipulate distributions, as it appears to take into account the characteristics (like modes, shape, etc) of both the source and the target distribution, and the resulting barycenter looks like a distribution combining those into one distribution, while the  $l_2$  barycenter does not merge those specificities into one distribution but rather re-normalize the source and target distributions.

## B. Remerciements et Contexte

### Institutionnel et Social du Stage

J'ai effectué mon stage dans l'équipe EMPENN (*cerveau* en breton) hébergée à l'IRISA à Rennes. L'équipe regroupe des personnels de l'INRIA, du CNRS, de l'INSERM, et de l'Université de Rennes 1. Je remercie de nouveau Pierre et Julie pour leur encadrement, et tous leurs conseils et éclairages, Armelle pour toute son aide et ses réponses à toutes mes questions, et puis tout le reste de



l'équipe encore avec qui j'ai passé d'excellents mois dans la ville de Rennes qu'elle a su me faire découvrir sous son meilleur jour.

J'ai pu, pendant les premiers mois du stage, participer à la vie de l'équipe, tant à travers ses séminaires réguliers, des répétitions de thèses, et puis plus informellement tout au cours des repas, des pauses à la cafétéria, des quiz du lundi soir, des trajets jusqu'au RU. J'ai également eu l'opportunité de prévoir une participation à la *Semaine du Cerveau* à travers une intervention lors d'un *Bar en (neuro)sciences*, bien qu'elle n'ait finalement pas eu lieu pour les raisons sanitaires que l'on sait bien.

## References

- [1] Olaf Sporns, Giulio Tononi, and Rolf Kötter. "The human connectome: a structural description of the human brain". In: *PLoS computational biology* 1.4 (2005) (cited on page 3).
- [2] David C Van Essen et al. "The WU-Minn human connectome project: an overview". In: *Neuroimage* 80 (2013), pp. 62–79 (cited on page 5).
- [3] Danielle S. Bassett et al. "Hierarchical organization of human cortical networks in health and schizophrenia." In: *The Journal of neuroscience : the official journal of the Society for Neuroscience* 28 37 (2008), pp. 9239–48 (cited on page 5).
- [4] Julie Coloigner et al. "White matter connectivity analysis in patients suffering from depression." In: (2018) (cited on pages 5, 6, 13, 23, 24).
- [5] Nico U. F. Dosenbach et al. "Prediction of individual brain maturity using fMRI." In: *Science* 329 5997 (2010), pp. 1358–61 (cited on page 5).
- [6] Xin Wen et al. "Detecting the Information of Functional Connectivity Networks in Normal Aging Using Deep Learning From a Big Data Perspective". In: *Frontiers in Neuroscience*. 2019 (cited on page 5).
- [7] Manasij Venkatesh, Joseph Jaja, and Luiz Pessoa. "Comparing functional connectivity matrices: A geometry-aware approach applied to participant identification". In: *NeuroImage* 207 (Nov. 2019), p. 116398. doi: [10.1016/j.neuroimage.2019.116398](https://doi.org/10.1016/j.neuroimage.2019.116398) (cited on pages 5, 6).

- [8] S. M. Hadi Hosseini and Shelli R. Kesler. “Comparing connectivity pattern and small-world organization between structural correlation and resting-state networks in healthy adults”. In: *NeuroImage* 78 (2013), pp. 402–414 (cited on page 5).
- [9] Jil Meier et al. “A Mapping Between Structural and Functional Brain Networks”. In: *Brain connectivity* 6 4 (2016), pp. 298–311 (cited on page 5).
- [10] Basak Alper et al. “Weighted graph comparison techniques for brain connectivity analysis”. In: *CHI ’13*. 2013 (cited on page 6).
- [11] Vicente Ponsoda et al. “Structural brain connectivity and cognitive ability differences: A multivariate distance matrix regression analysis”. In: *Human Brain Mapping* 38 (2017), pp. 803–816 (cited on page 6).
- [12] Emily S. Finn et al. “Functional connectome fingerprinting: Identifying individuals based on patterns of brain connectivity”. In: *Nature Neuroscience*. 2015 (cited on page 6).
- [13] Mikail Rubinov and Olaf Sporns. “Complex network measures of brain connectivity: Uses and interpretations”. In: *NeuroImage* 52 (2010), pp. 1059–1069 (cited on page 6).
- [14] Ahmad Mheich, Fabrice Wendling, and Mahmoud Hassan. “Brain network similarity: Methods and applications.” In: 2019 (cited on page 6).
- [15] Jie Xiang et al. “Graph-based network analysis of resting-state fMRI: test-retest reliability of binarized and weighted networks”. In: *Brain Imaging and Behavior* (2019), pp. 1–12 (cited on page 7).
- [16] Benjamin Ricaud et al. “Fourier could be a data scientist: From graph Fourier transform to signal processing on graphs”. In: *Comptes Rendus Physique* 20.5 (2019), pp. 474–488 (cited on page 7).
- [17] Xiaowen Dong et al. “Learning Laplacian Matrix in Smooth Graph Signal Representations”. In: *IEEE Transactions on Signal Processing* 64 (Dec. 2016), pp. 1–1. DOI: [10.1109/TSP.2016.2602809](https://doi.org/10.1109/TSP.2016.2602809) (cited on page 12).
- [18] Hermina Petric Maretic et al. “GOT: An Optimal Transport framework for Graph comparison”. In: *Advances in Neural Information Processing Systems*. 2019, pp. 13876–13887 (cited on pages 12, 13, 18, 24).

- [19] Rajendra Bhatia, Tanvi Jain, and Yongdo Lim. “On the Bures–Wasserstein distance between positive definite matrices”. In: *Expositiones Mathematicae* 37.2 (2019), pp. 165–191 (cited on pages 13, 15).
- [20] Gabriel Peyré, Marco Cuturi, et al. “Computational optimal transport”. In: *Foundations and Trends® in Machine Learning* 11.5–6 (2019), pp. 355–607 (cited on pages 15, 27).
- [21] Pedro C. Álvarez-Esteban et al. “A fixed-point approach to barycenters in Wasserstein space”. In: 2015 (cited on pages 15, 16).
- [22] Chien-Chun Ni et al. “Ricci curvature of the internet topology”. In: 2015 *IEEE Conference on Computer Communications (INFOCOM)*. IEEE. 2015, pp. 2758–2766 (cited on page 18).
- [23] Jayson Sia, Edmond Jonckheere, and Paul Bogdan. “Ollivier-ricci curvature-based method to community detection in complex networks”. In: *Scientific reports* 9.1 (2019), pp. 1–12 (cited on page 18).
- [24] Hamza Farooq et al. “Network curvature as a hallmark of brain structural connectivity”. In: *Nature Communications*. 2019 (cited on pages 18, 23–25).
- [25] Yann Ollivier. “Ricci curvature of Markov chains on metric spaces”. In: *Journal of Functional Analysis* 256.3 (2009), pp. 810–864 (cited on pages 20, 21).
- [26] Max-K. von Renesse and K. Sturm. “Transport inequalities, gradient estimates, entropy and Ricci curvature”. In: 2005 (cited on page 21).
- [27] Chien-Chun Ni et al. “Community detection on networks with ricci flow”. In: *Scientific reports* 9.1 (2019), pp. 1–12 (cited on pages 22, 25).
- [28] Frank Bauer, Jurgen Jost, and Shiping Liu. “Ollivier-Ricci curvature and the spectrum of the normalized graph Laplace operator”. In: 2011 (cited on page 22).
- [29] Ai Wern Chung et al. “Characterising brain network topologies: a dynamic analysis approach using heat kernels”. In: *Neuroimage* 141 (2016), pp. 490–501 (cited on page 23).

- [30] Peter A. Robinson. “Interrelating anatomical, effective, and functional brain connectivity using propagators and neural field theory.” In: *Physical review. E, Statistical, nonlinear, and soft matter physics* 85 1 Pt 1 (2012), p. 011912 (cited on page 23).
- [31] P. A. Robinson et al. “Determination of effective brain connectivity from functional connectivity with application to resting state connectivities”. In: *Phys. Rev. E* 90 (1 July 2014), p. 012707. DOI: [10.1103/PhysRevE.90.012707](https://doi.org/10.1103/PhysRevE.90.012707) (cited on page 23).
- [32] Melanie Weber, Jürgen Jost, and Emil Saucan. “Forman-Ricci flow for change detection in large dynamic data sets”. In: *Axioms* 5.4 (2016), p. 26 (cited on page 25).
- [33] Cédric Villani. *Topics in optimal transportation*. 58. American Mathematical Soc., 2003 (cited on page 28).